

This is the accepted manuscript made available via CHORUS. The article has been published as:

Strong spin-orbit coupling and Dirac nodal lines in the three-dimensional electronic structure of metallic rutile  $\text{IrO}_2$

X. Xu, J. Jiang, W. J. Shi, Vicky Süß, C. Shekhar, S. C. Sun, Y. J. Chen, S.-K. Mo, C. Felser, B. H. Yan, H. F. Yang, Z. K. Liu, Y. Sun, L. X. Yang, and Y. L. Chen

Phys. Rev. B **99**, 195106 — Published 3 May 2019

DOI: [10.1103/PhysRevB.99.195106](https://doi.org/10.1103/PhysRevB.99.195106)

# Strong Spin-Orbit Coupling and Dirac Nodal-lines in Three Dimensional Electronic Structure of Metallic Rutile IrO<sub>2</sub>

X. Xu<sup>\*1</sup>, J. Jiang<sup>\*2,3,4</sup>, W. J. Shi<sup>5</sup>, Vicky Süß<sup>5</sup>, C. Shekhar<sup>5</sup>, S. C. Sun<sup>1</sup>, Y. J. Chen<sup>1</sup>, S.-K. Mo<sup>4</sup>, C. Felser<sup>5</sup>, B. H. Yan<sup>5</sup>, H. F. Yang<sup>2</sup>, Z. K. Liu<sup>2</sup>, Y. Sun<sup>5</sup>, L. X. Yang<sup>†1,6</sup> and Y. L. Chen<sup>†1,2,3</sup>

<sup>1</sup>State Key Laboratory of Low Dimensional Quantum Physics, Department of Physics, Tsinghua University, Beijing 100084, P. R. China

<sup>2</sup>School of Physical Science and Technology, ShanghaiTech University, Shanghai, P. R. China

<sup>3</sup>Department of Physics, University of Oxford, Oxford, OX1 3PU, UK

<sup>4</sup>Advanced Light Source, Lawrence Berkeley National Laboratory, Berkeley, CA 94720, USA

<sup>5</sup>Max Planck Institute for Chemical Physics of Solids, D-01187 Dresden, Germany

<sup>6</sup>Collaborative Innovation Center of Quantum Matter, Beijing 100084, P. R. China

*\*These authors contribute equally to this work.*

*†Email: lxyang@tsinghua.edu.cn, yulin.chen@physics.ox.ac.uk*

Using high-resolution angle-resolved photoemission spectroscopy and *ab initio* calculation, we have studied the bulk and surface electronic structure of metallic rutile 5d transition metal oxide IrO<sub>2</sub> that harbours both edge and corner sharing Ir-O octahedrons. We observe strong modulation of the band structure by spin-orbit coupling (SOC). The measured band structure is well reproduced by our *ab initio* calculation without band renormalization, suggesting the absence of the SOC-enhanced correlation effect in IrO<sub>2</sub>. In accordance with the calculation, we visualize two types of Dirac nodal lines (DNLs) protected by mirror symmetry and non-symmorphic crystal symmetry respectively. SOC gaps the first type of DNLs, which may contribute largely to the strong spin Hall effect. The second type of DNLs at the edges of Brillouin zone, however, remain intact against SOC. Our results not only provide important insights into the exotic transport properties of IrO<sub>2</sub>, but also shed light on the understanding of the role of SOC in the iridate family.

## I. INTRODUCTION

Iridates represent a particular family of transition metal oxides with rich and fascinating properties such as metal insulator transition [1-3], cuprate-like behaviours [4-6], unusual magnetism [7-9], spin liquid behaviour [10, 11], and quantum topological phases [12-14]. Behind these intriguing phenomena, strong spin-orbit coupling (SOC) from heavy iridium atoms is believed to play decisive roles. However, it is challenging to unveil the specific role of SOC in the physical properties by experimental techniques without momentum resolution such as transport measurement. Instead, SOC effect is usually manifested by strong modulation of the electronic structure. A prime example is the band narrowing by exotic  $J_{\text{eff}} = 1/2$  ground state in  $\text{Sr}_2\text{IrO}_4$  due to the SOC-enhanced electron correlation, which lead to an exotic Mott insulator state [4, 6]. In order to further understand the role of SOC in the physics of iridates, it is highly demanded to investigate the modification of their electronic structures by strong SOC.

Among the family of iridates, the rutile oxide  $\text{IrO}_2$  has attracted great research attention. It has the simplest binary chemical composition without extra metal cations in the iridate system, which provides an ideal platform to explore the intrinsic SOC effect from Ir atoms. Although the role of strong SOC in  $\text{IrO}_2$  has been widely proven by various experimental results, such as optical spectroscopy [15], x-ray absorption spectroscopy [16], angle-resolved photoemission spectroscopy (ARPES) [17-19] and resonant x-ray diffraction experiment [20], there is still heavy debate regarding the existence of SOC-enhanced  $J_{\text{eff}} = 1/2$  state in the metallic  $\text{IrO}_2$  [16, 20-22]. Interestingly,  $\text{IrO}_2$  exhibits strong spin Hall effect [23], which is still barely understood. Theoretical calculation has predicted the existence of multiple Dirac nodal lines (DNLs) in  $\text{IrO}_2$  and suggested their close connection with the observed spin Hall effect [24], which proposes further experimental and theoretical investigation of its electronic structure. Moreover,  $\text{IrO}_2$

promises broad application potentials such as spin valves and spin detectors in spintronics [25], oxygen barriers and electrodes in memory devices [26], and stable water splitting catalyst in electrochemical [27]. It is thus of great interest and importance to investigate the three dimensional (3D) electronic structure of IrO<sub>2</sub> in order to further understand the role of SOC and predicted DNLs in its physical properties.

Based on the above motivation, in this work, we comprehensively investigate the 3D electronic structure of IrO<sub>2</sub> using high-resolution ARPES and *ab-initio* calculation. The energy bands over the 3D Brillouin zone (BZ) show very weak electronic correlation, although the SOC induces clear energy gaps in the band structure, suggesting the absence of SOC-enhanced electron correlation in IrO<sub>2</sub>. Moreover, we identify two types of DNLs and surface states that may be crucial for the transport properties of IrO<sub>2</sub>. Our results will not only help understand the exotic electronic properties of IrO<sub>2</sub>, but also shed light on the comprehension of the interplay between electronic correlation, strong SOC, and lattice structure in *5d* transition metal oxides.

## II. EXPERIMENT

High quality IrO<sub>2</sub> single crystals were synthesized by flux method [28]. ARPES measurements were performed at the beamline 4.0.3 and beamline 10.0.1 of the Advance Light Source (ALS), and beamline I05 of the Diamond Light Source (DLS) with an overall energy resolution better than 20 meV and a base pressure better than  $1.5 \times 10^{-10}$  Torr. Density functional theory (DFT) calculations were performed using the Vienna *ab-initio* Simulation Package (VASP) [29] with a plane wave basis. The interactions between the valence electrons and ion cores were described using the projector augmented wave method. The exchange and correlation energy were formulated using the generalized gradient approximation with the Perdew-Burke-Ernzerhof (PBE) scheme. The plane-wave basis cut off energy was set to 500 eV.  $\Gamma$ -centered k points with

a spacing of  $0.03 \text{ \AA}^{-1}$  were used for the first BZ sampling. The local density of states (LDOS) is relative to the image part of the semi-infinite surface Green's function based on the tight binding Hamiltonian. The tight-binding Hamiltonian was constructed by projecting the Bloch states into the atomic orbital like Wannier function supplied by the Wannier 90 code.

### III. RESULTS AND DISCUSSION

$\text{IrO}_2$  single crystal crystallizes into the rutile-type structure with lattice constants  $a = b = 4.498 \text{ \AA}$  and  $c = 3.154 \text{ \AA}$  (space group  $P4_2/mnm$ , No.136), as shown in Figs. 1(a) and 1(b) [28]. It shares the common  $\text{IrO}_6$  octahedrons as the basic structure component, similar to other iridium oxides. The  $\text{IrO}_6$  octahedrons stack in a body-centered structure, forming both corner and edge sharing networks. It can be naturally cleaved along the (110) direction, inducing clean sample surface for ARPES measurements (see Supplemental Material [30]). Fig. 1(c) shows core-level photoemission spectrum of  $\text{IrO}_2$  with clear Ir  $4f$  and  $5p$  peaks. Intensity of the valence bands in Fig. 1(c) is magnified by a factor of ten to reveal the diversity of Ir  $5d$  components near the Fermi level, which is key to most of its physical properties as well as chemical applications such as stable high-efficiency catalyst for water splitting [31].

According to our *ab-initio* calculations,  $\text{IrO}_2$  harbours two types of DNLs without SOC as indicated by blue and green curves in Fig. 1(d). It should be highlighted that crystalline symmetries, shown in Figs. 1(a) and 1(b), play an important role in forming DNLs. The first type of DNLs originates from the anti-crossing of  $d_{x^2-y^2}$  and  $d_{xz, yz}$  bands and is protected by mirror symmetry along (110) and  $(\bar{1}\bar{1}0)$  planes marked by  $m(110)$  and  $m(\bar{1}\bar{1}0)$  in Fig. 1(b). They disperse within (110) and  $(\bar{1}\bar{1}0)$  mirror planes in BZ and form hextuple points (HP) and octuplet points (OP) along  $\Gamma Z$  and AM directions respectively as shown in Fig. 1(e). The second type of

DNLs is promised by the non-symmorphic symmetry including a fourfold screw rotation around z-axis  $\tilde{C}_{4z}$  and a glide mirror reflection along (100) and (010) planes [ $\tilde{m}(100)$  and  $\tilde{m}(010)$ ]. Strong SOC gaps the first type of DNLs, while the second type of DNLs survive along AM and MX directions [24]. Figures 1(e) and 1(f) show the calculated band dispersions along high symmetry directions with and without SOC, respectively. SOC lifts the band degeneracy and induces energy gaps at the HP and OP, which are ideal indicators for the modulation of the electronic structure by SOC.

The corresponding 3D BZ and its projected (110) surface BZ are presented in Fig. 2(a) with high symmetry points indicated. According to our theoretical calculation, the Fermi surface (FS) consists of crossed concentric-reducer-like structure (FS1) along the ZR direction (brown pockets in Fig. 2(b)) and a nearly flat structure (FS2) parallel to the RAMX plane (cyan pockets in Fig. 2(b)), as well as an ellipsoid (FS3) near the M point (green pockets in Fig. 2(b)). Notably, both FS1 and FS2 are open FSs, which may play important roles in transport properties of IrO<sub>2</sub> under high magnetic field [32]. Figures 2(c)-2(e) show the calculated bulk FS's at different  $k_z$ 's. In the  $\Gamma$ ZAM plane ( $k_z = 0$ ), there exist a circular pocket  $\alpha$  centered at Z, an elliptical pocket  $\delta$  centered at M and a “dog-bone” like pocket  $\beta$  at A. The  $\beta$  and  $\delta$  pockets are degenerate along AM due to the DNL protected by the non-symmorphic crystal symmetry. The FSs show strong  $k_z$  variation. In the XRRX plane (Fig. 2(d)), we observe a large elliptical pocket  $\gamma$  at R and a racetrack-like pocket  $\eta$  at X. Since the sample is cleaved along (110) direction, the FS's at  $k_z = 0$  and  $k_z = \pi/d$  ( $d = \sqrt{2}a/2$  is the interlayer distance along (110) direction) have the same structure. In order to experimentally visualize the 3D bulk FS, we conduct photon energy dependent ARPES experiment. The FSs measured at 122 eV, 138 eV and 164 eV are presented in Figs. 2(f)-(h), which correspond to  $k_z = 0$ ,  $\pi/2d$  and  $\pi/d$ , respectively (see Supplemental Material [30]).

Due to the limited  $k_z$  resolution and the strong  $k_z$  dispersion of the bulk bands, the measured FS is strongly complicated by the projected features from different  $k_z$ 's. Nevertheless, we can still distinguish the FS sheets, such as  $\alpha$ ,  $\beta$ ,  $\delta$  and  $\gamma$  pockets. Our experiment and calculation show overall agreement, including the Fermi pocket positions and sizes.

Figures 2(i) and 2(j) show band dispersions along high symmetry directions. For a direct comparison, we superimpose the calculated bulk bands on top of the experiments without renormalization. We observe a good agreement between experiment and calculation in a large energy range, suggesting very weak correlation effect in IrO<sub>2</sub>. In consistence with the calculation, the first type of DNLs that are protected by mirror symmetry are indeed gapped by strong SOC effect and the predicted energy gaps induced by SOC are directly observed along both  $\Gamma Z$  and  $AM$  as indicated in Figs. 2(i) and 2(j). It is proposed that the SOC-gapped DNLs play decisive roles in the strong spin Hall effect in IrO<sub>2</sub>, the mechanism of which calls for further investigation [23]. The gap at HP introduces a unique electronic structure with an energy band dispersing through the gap and connecting the upper and lower part of the gapped band (Fig. 2(i)), in good agreement with calculation. The observed weak correlation effect and strong SOC effect suggest the absence of the SOC-enhanced correlation effect in IrO<sub>2</sub>.

In order to further unveil the fine electronic structure of IrO<sub>2</sub>, we conduct ARPES measurements using lower photon energy with enhanced energy resolution in Fig. 3. Due to the surface sensitivity of low energy photons, the ARPES spectra are dominated by the photoelectrons from the surface. Thus we use the surface BZ (Black rectangles in Fig. 3) to illustrate the in-plane electronic structures. The band structure measured with photons at 80 eV (near  $k_z = \pi/d$ ) is presented in a 3D plot in Fig. 3(a). The high quality of our data enables us to resolve the details of the electronic structure. We reveal an arc-like structure  $\delta$  centered at  $\bar{\Gamma}$ , a

“dog-bone” like electron pocket  $\beta$  at  $\bar{Y}$  and a hole pocket  $\gamma$  at  $\bar{M}$  from the constant energy contours at  $E_F$  and 150 meV as shown in Figs. 3(b) and 3(d), which are well reproduced by the surface projected band calculations in Figs. 3(c) and 3(e). The band dispersions along different cuts are plotted in Figs. 3(f) and 3(g). The side-by-side comparison between experiment and calculation again shows good agreement, in consistence with the weak correlation effect in IrO<sub>2</sub>. In addition to the bulk states, the enhanced surface sensitivity enables us to observe the surface states [marked as SS<sub>1</sub> and SS<sub>2</sub> in Figs. 3(b) and 3(c)], which are well captured by our calculations. SS<sub>2</sub> disperses strongly along the edge sharing IrO<sub>6</sub> chains, while SS<sub>1</sub> shows shallow dispersions along both  $\bar{\Gamma}\bar{Y}$  and  $\bar{\Gamma}\bar{X}$ . The origin of these surface states and their possible roles in the transport properties of IrO<sub>2</sub> deserve further studies.

According to *ab initio* calculations, there exist DNLs protected by the non-symmorphic crystal structure of IrO<sub>2</sub> even under strong SOC, as shown in Fig. 1(c) and schematically illustrated in Figs. 4(a) and 4(d). In order to visualize the DNLs, we show the dispersions along MA and XM using 164 eV and 80 eV respectively in Figs. 4(b) and 4(e). We directly observe the dispersion of the DNL along MA (Fig. 4(b)). The dispersions perpendicular to the DNL along MA are shown in Fig. 4(c), which clearly show the evolution of the Dirac points along the DNL. In addition to the DNL along MA, we also observe the projection of the nodal line along MX on the  $\Gamma$ MZ plane. Figure 4(d) schematically shows the calculated nodal line along MX direction. We observe the projection of this nodal line into the  $\Gamma$ MZ plane as shown in Fig. 4(e). Figure 4(f) shows the evolution of the dispersions perpendicular to the nodal line, which verifies the existence of Dirac points. Detailed analysis of the second type of DNLs is also delivered in Supplemental Material [30]. Up to date, DNLs protected by non-symmorphic symmetry are widely observed in different systems [33]. However, the DNLs usually resides far away from  $E_F$ .



For example, similar DNLs have been observed by ARPES in ZrSiS [34, 35] and InBi [36], which are hundreds of meV away from Fermi level. In contrast, the DNLs in IrO<sub>2</sub> cross Fermi level, which provides an ideal platform to realize possible application of DNLs.

Recently, two analogous types of DNLs have been experimentally observed in RuO<sub>2</sub> that is isostructural with IrO<sub>2</sub> [37]. Two points should be noted concerning the similarities and differences of the DNL properties in RuO<sub>2</sub> and IrO<sub>2</sub>: (i) Despite the overall similarity of band structures, the chemical potential in IrO<sub>2</sub> is relatively higher than that in RuO<sub>2</sub> by about 600 meV due to the different electron filling level [24, 38]. Thus, the energy of the first type of DNL, which is slightly gapped by SOC, is much higher than the Fermi level, leading to a minor influence upon the exotic transport properties such as spin Hall effect in RuO<sub>2</sub>. By contrast, both types of DNLs in IrO<sub>2</sub> directly cross the Fermi level, which not only result in the strong spin Hall effect [23], but may also contribute to other novel transport phenomena such as 3D quantum Hall effect [39]. (ii) In comparison with IrO<sub>2</sub>, the SOC is relatively weak and negligible in RuO<sub>2</sub>, giving rise to the observation of an additional type of DNL (DNL3) in RuO<sub>2</sub> [37]. Indeed, in the absence of SOC, the non-symmorphic symmetry guarantees band degeneracies in the whole XMAR plane including the XR direction hosting DNL3 in RuO<sub>2</sub>. When the SOC is included, however, DNLs only survives along the edges of the BZ. Therefore, the DNL3 is largely gapped in IrO<sub>2</sub>, as revealed by both our calculation and photoemission results, which further emphasizes the importance of SOC in IrO<sub>2</sub>.

#### **IV. Summary**

To summarize, we have presented a comprehensive understanding of the 3D electronic structure of the rutile oxide IrO<sub>2</sub>. We observe strong modulation of the band structure by SOC, while the correlation effect is very weak suggesting the negligible impact of the SOC-enhanced

correlation effect in metallic IrO<sub>2</sub>. We directly visualize the DNLs that are protected by non-symmorphic crystal symmetry and identify surface states, which may be important to the intriguing transport properties of IrO<sub>2</sub>. Our results provide important insights into the modulation of the band structure of iridium oxides by the SOC and crystal symmetry, which will shed light on the understanding of their exotic properties.

### **Acknowledgement**

This paper was supported by the National Natural Science Foundation of China (Grants No. 11774190 & No. 11674229), the National Key R&D program of China (Grants No. 2017YFA0304600, No. 2017YFA0305400 and No. 2017YFA0402900), the EPSRC (UK) Platform Grant (Grant No. EP/M020517/1). This research used resources of the Advanced Light Source, which is a DOE Office of Science User Facility under contract no. DE-AC02-05CH11231.

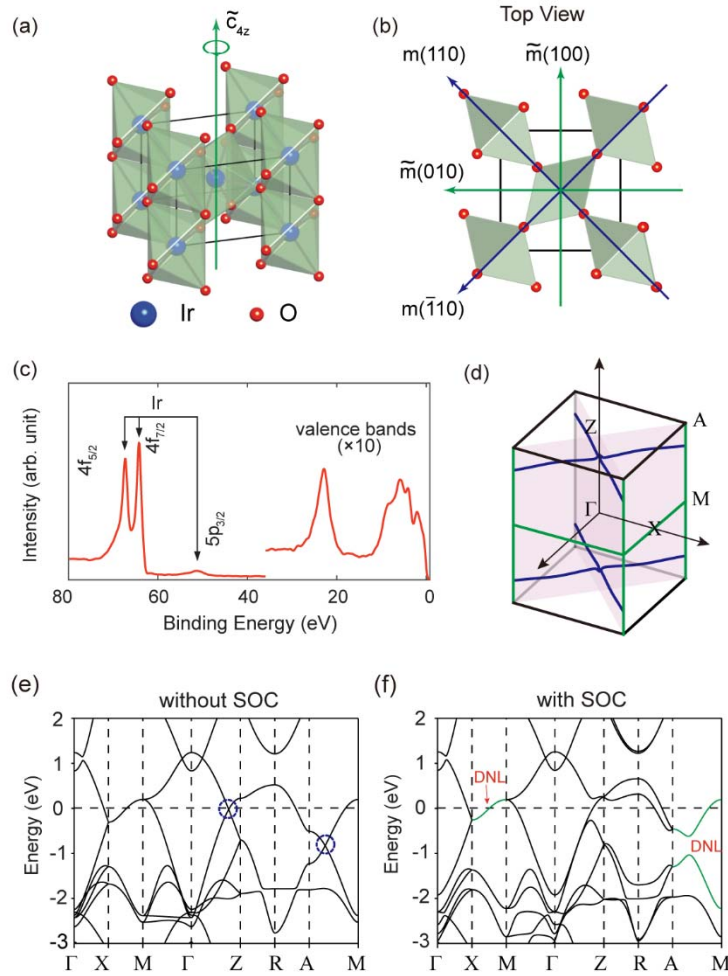


**Fig.1 Overview of the crystalline symmetry of IrO<sub>2</sub> and band structure** (a) Bird-eye view and (b) Top view of crystal structure of IrO<sub>2</sub>. Critical symmetry operations are indicated upon the lattice. (c) Core-level photoemission spectrum clearly showing Iridium 4*f* and 5*p* peaks. (d) Theoretically predicted DNLs in three-dimensional (3D) Brillouin zone (BZ) of IrO<sub>2</sub> [first type of Dirac nodal lines (DNLs) in blue, while second type of DNLs in green]. The light purple planes indicate the mirror planes. (e), (f) Calculated bulk electronic structure of IrO<sub>2</sub> (e) without and (f) with spin-orbit coupling. Blue dotted circles and green lines indicate the position of DNLs.

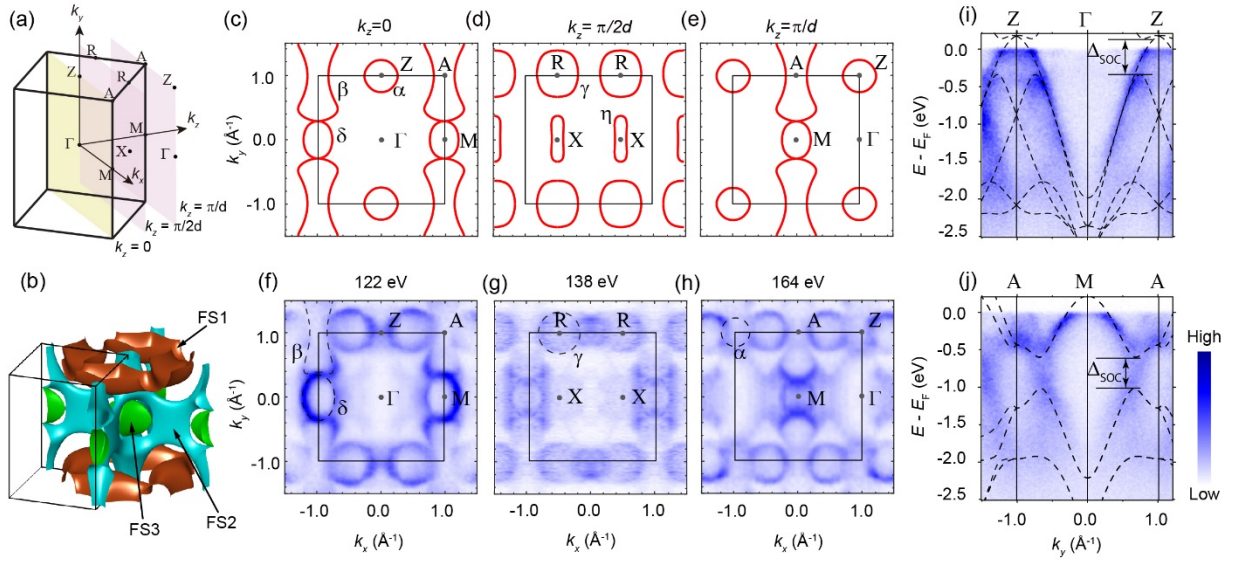


**Fig.2 Three-dimensional electronic structure of IrO<sub>2</sub>** (a) Illustration of the 3D BZ of IrO<sub>2</sub>, with the indication of planes at  $k_z = 0$ ,  $k_z = \pi/2d$ , and  $k_z = \pi/d$ . (b) Calculated Fermi surface structure of IrO<sub>2</sub>. (c-e) Calculated bulk FS at  $k_z = 0$  (f),  $k_z = \pi/2d$  (g) and  $k_z = \pi/d$  (h). (f-h) Photoemission intensity map in  $k_x$ - $k_y$  plane obtained at different photon energies. (i), (j) Measured band dispersion along  $Z\Gamma Z$  (i) and  $AMA$  (j) directions. The calculated bulk band structure (dashed lines) are overlaid for comparison. Data were collected at 10 K.

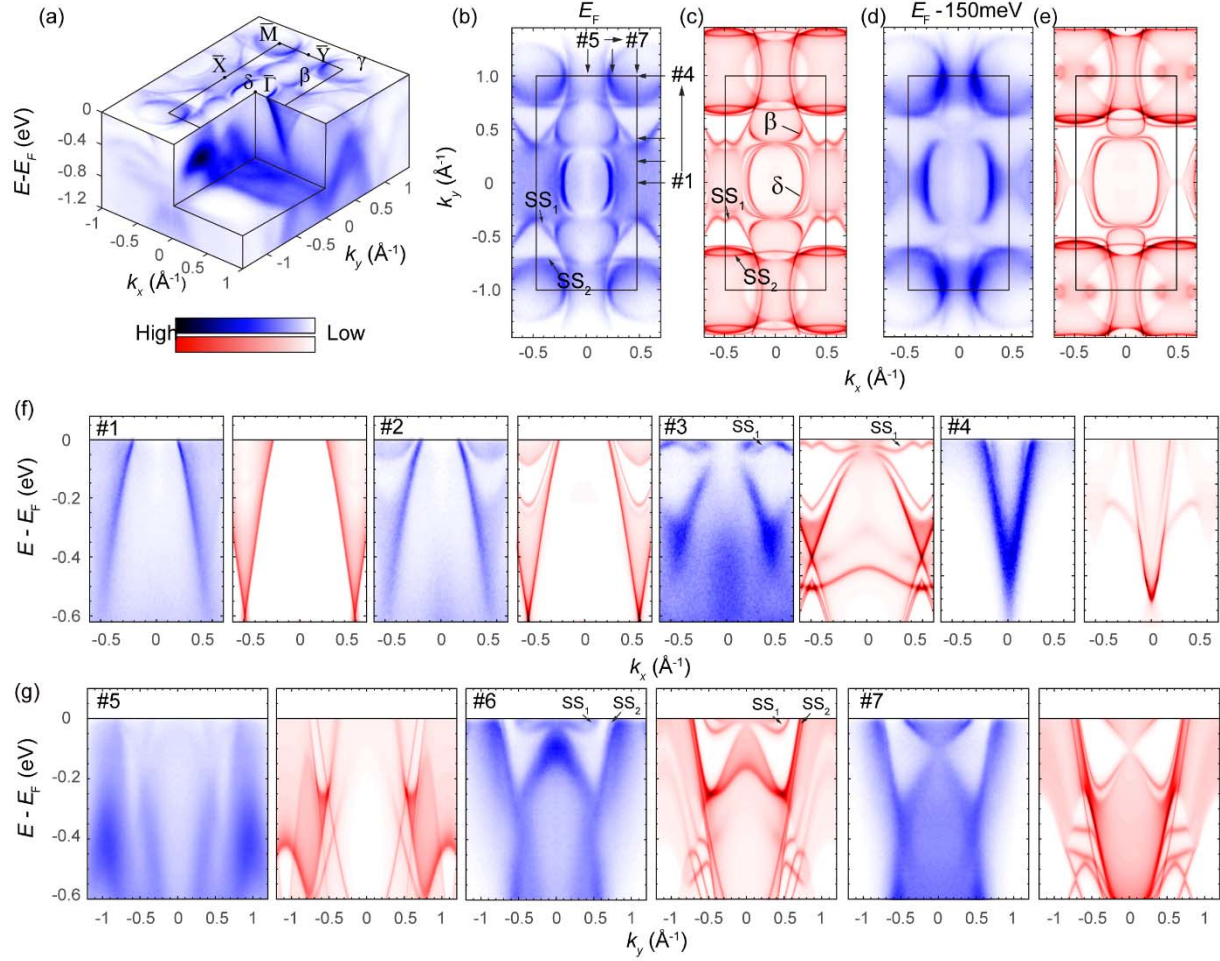


**Fig.3 Details of the electronic structure of IrO<sub>2</sub>** (a) 3D plot of the band structure of IrO<sub>2</sub> measured with 80 eV photons. (b-e) Comparison between experimental (b, d) and calculated (c, e) constant energy contours at different binding energies. (f), (g) Comparison between experimental and calculated band dispersions along different cuts that are parallel to  $k_x$  and  $k_y$ , as indicated in panel (b). The experimental and calculated data are shown in blue and red false-color plots, respectively. Data were symmetrized along  $\bar{\Gamma X}$  and  $\bar{\Gamma Y}$  for a better comparison with calculation.

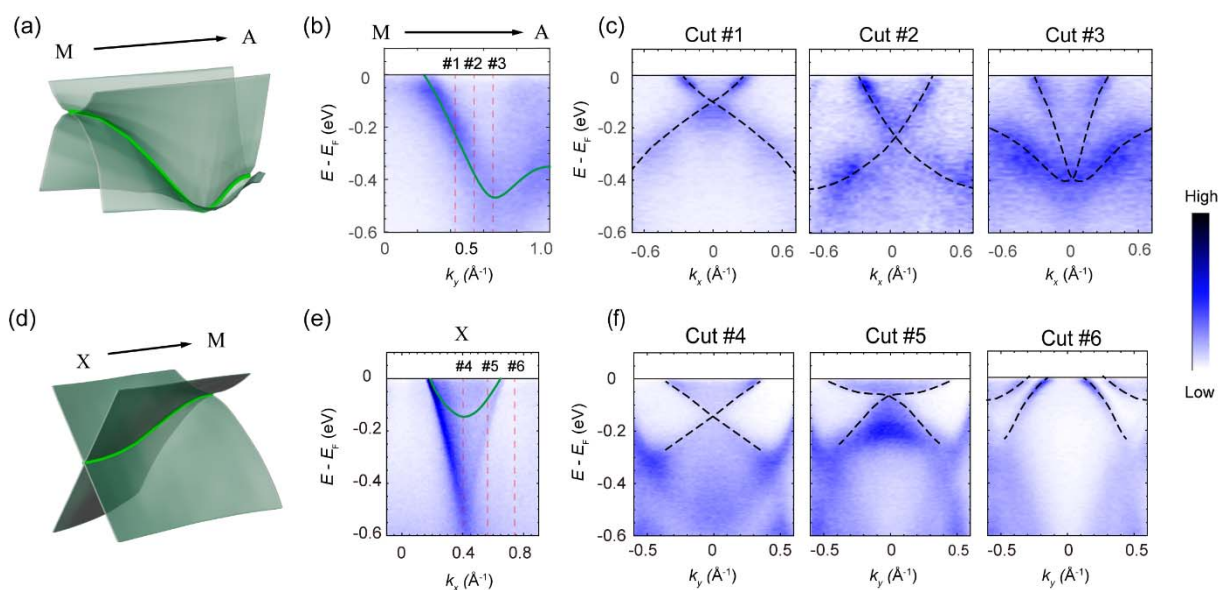


**Fig.4 The second type of DNLs protected by non-symmorphic crystal symmetries.** (a) 3D illustration of the calculated Dirac nodal line along MA direction in IrO<sub>2</sub>. (b) Band dispersion along MA direction. The green curve indicates the calculated nodal line. (c) Band dispersions along different momentum cuts perpendicular to the MA direction, as indicated in panel (b). (d) 3D illustration of the calculated Dirac nodal line along MX direction. (e) Band dispersion along MX. The green curve indicates the calculated nodal line. (f) Band dispersions along different momentum cuts perpendicular to the MX direction, as indicated in panel (e).

## References:

- [1] H. Zhang, K. Haule, D. Vanderbilt, *Phys. Rev. Lett.* 118, 026404 (2017).
- [2] Z. Tian, Y. Kohama, T. Tomita, H. Ishizuka, T.H. Hsieh, J.J. Ishikawa, K. Kindo, L. Balents, S. Nakatsuji, *Nat. Phys.* 12, 134 (2015).
- [3] S.H. Chun, B. Yuan, D. Casa, J. Kim, C.-Y. Kim, Z. Tian, Y. Qiu, S. Nakatsuji, Y.-J. Kim, *Phys. Rev. Lett.* 120, 177203 (2018).
- [4] B.J. Kim, H. Ohsumi, T. Komesu, S. Sakai, T. Morita, H. Takagi, T. Arima, *Science* 323, 1329-1332 (2009).
- [5] Y.K. Kim, O. Krupin, J.D. Denlinger, A. Bostwick, E. Rotenberg, Q. Zhao, J.F. Mitchell, J.W. Allen, B.J. Kim, *Science* 345, 187-190 (2014).
- [6] B.J. Kim, H. Jin, S.J. Moon, J.Y. Kim, B.G. Park, C.S. Leem, J. Yu, T.W. Noh, C. Kim, S.J. Oh, J.H. Park, V. Durairaj, G. Cao, E. Rotenberg, *Phys. Rev. Lett.* 101, 076402 (2008).
- [7] J. Chaloupka, G. Jackeli, G. Khaliullin, *Phys. Rev. Lett.* 105, 027204 (2010).
- [8] G. Jackeli, G. Khaliullin, *Phys. Rev. Lett.* 102, 017205 (2009).
- [9] M.A. Laguna-Marco, D. Haskel, N. Souza-Neto, J.C. Lang, V.V. Krishnamurthy, S. Chikara, G. Cao, M. van Veenendaal, *Phys. Rev. Lett.* 105, 216407 (2010).
- [10] T. Dey, A.V. Mahajan, P. Khuntia, M. Baenitz, B. Koteswararao, F.C. Chou, *Phys. Rev. B* 86, 140405 (2012).
- [11] M.J. Lawler, A. Paramakanti, Y.B. Kim, L. Balents, *Phys. Rev. Lett.* 101, 197202 (2008).
- [12] M.C. Shapiro, S.C. Riggs, M.B. Stone, C.R. de la Cruz, S. Chi, A.A. Podlesnyak, I.R. Fisher, *Phys. Rev. B* 85, 214434 (2012).
- [13] X. Wan, A.M. Turner, A. Vishwanath, S.Y. Savrasov, *Phys. Rev. B* 83, 205101 (2011).
- [14] A. Shitade, H. Katsura, J. Kuneš, X.-L. Qi, S.-C. Zhang, N. Nagaosa, *Phys. Rev. Lett.* 102, 256403 (2009).
- [15] J. de Almeida, R. Ahuja, *Phys. Rev. B* 73, 165102 (2006).
- [16] J.P. Clancy, N. Chen, C.Y. Kim, W.F. Chen, K.W. Plumb, B.C. Jeon, T.W. Noh, Y.-J. Kim, *Phys. Rev. B* 86, 195131 (2012).
- [17] J.K. Kawasaki, M. Uchida, H. Paik, D.G. Schlom, K.M. Shen, *Phys. Rev. B* 94, 121104 (2016).
- [18] P.K. Das, J. Sławińska, I. Vobornik, J. Fujii, A. Regoutz, J.M. Kahk, D.O. Scanlon, B.J. Morgan, C. McGuinness, E. Plekhanov, D. Di Sante, Y.-S. Huang, R.-S. Chen, G. Rossi, S. Picozzi, W.R. Branford, G. Panaccione, D.J. Payne, *Phys. Rev. Mat.* 2, 065001 (2018).
- [19] J.K. Kawasaki, C.H. Kim, J.N. Nelson, S. Crisp, C.J. Zollner, E. Biegenwald, J.T. Heron, C.J. Fennie, D.G. Schlom, K.M. Shen, *Phys. Rev. Lett.* 121, 176802 (2018).
- [20] Y. Hirata, K. Ohgushi, J.-i. Yamaura, H. Ohsumi, S. Takeshita, M. Takata, T.-h. Arima, *Phys. Rev. B* 87, 161111 (2013).
- [21] S.K. Panda, S. Bhowal, A. Delin, O. Eriksson, I. Dasgupta, *Phys. Rev. B* 89, 155102 (2014).
- [22] W.J. Kim, S.Y. Kim, C.H. Kim, C.H. Sohn, O.B. Korneta, S.C. Chae, T.W. Noh, *Phys. Rev. B* 93, 045104 (2016).
- [23] K. Fujiwara, Y. Fukuma, J. Matsuno, H. Idzuchi, Y. Niimi, Y. Otani, H. Takagi, *Nat Commun* 4, 2893 (2013).
- [24] Y. Sun, Y. Zhang, C.-X. Liu, C. Felser, B. Yan, *Phys. Rev. B* 95, 235104 (2017).
- [25] K. Fujiwara, Y. Fukuma, J. Matsuno, H. Idzuchi, Y. Niimi, Y. Otani, H. Takagi, *Nat Commun.* 4, 2893 (2013).
- [26] Y.J. Song, H.H. Kim, S.Y. Lee, D.J. Jung, B.J. Koo, J.K. Lee, Y.S. Park, H.J. Cho, S.O.

- Park, K. Kim, *Appl. Phys. Lett.* 76, 451-453 (2000).
- [27] C.C.L. McCrory, S. Jung, J.C. Peters, T.F. Jaramillo, *J. Am. Chem. Soc.* 135, 16977-16987 (2013).
- [28] S.R. Butler, J.L. Gillson, *Mater. Res. Bull.* 6, 81-89 (1971).
- [29] G. Kresse, J. Furthmüller, *Phys. Rev. B* 54, 11169-11186 (1996).
- [30] See Supplementary Material at [URL to be inserted] for (I) Sample characterization, (II) kz-dispersion of IrO<sub>2</sub>, and (III) detailed analysis of the second type of Dirac nodal lines.
- [31] Y. Ping, G. Galli, W.A. Goddard, *The Journal of Physical Chemistry C* 119, 11570-11577 (2015).
- [32] J.J. Lin, S.M. Huang, Y.H. Lin, T.C. Lee, H. Liu, X.X. Zhang, R.S. Chen, Y.S. Huang, *Journal of Physics: Condensed Matter* 16, 8035 (2004).
- [33] S.-Y. Yang, H. Yang, E. Derunova, S.S.P. Parkin, B. Yan, M.N. Ali, *Advances in Physics: X* 3, 1414631 (2018).
- [34] C. Chen, X. Xu, J. Jiang, S.C. Wu, Y.P. Qi, L.X. Yang, M.X. Wang, Y. Sun, N.B.M. Schröter, H.F. Yang, L.M. Schoop, Y.Y. Lv, J. Zhou, Y.B. Chen, S.H. Yao, M.H. Lu, Y.F. Chen, C. Felser, B.H. Yan, Z.K. Liu, Y.L. Chen, *Phys. Rev. B* 95, 125126 (2017).
- [35] L.M. Schoop, M.N. Ali, C. Straßer, A. Topp, A. Varykhalov, D. Marchenko, V. Duppel, S.S.P. Parkin, B.V. Lotsch, C.R. Ast, *Nat. Commun.* 7, 11696 (2016).
- [36] S.A. Ekahana, S.-C. Wu, J. Jiang, K. Okawa, D. Prabhakaran, C.-C. Hwang, S.-K. Mo, T. Sasagawa, C. Felser, B. Yan, Z. Liu, Y. Chen, *New Journal of Physics* 19, 065007 (2017).
- [37] V. Jovic, R.J. Koch, S.K. Panda, H. Berger, P. Bugnon, A. Magrez, K.E. Smith, S. Biermann, C. Jozwiak, A. Bostwick, E. Rotenberg, S. Moser, *Phys. Rev. B* 98, 241101 (2018).
- [38] L.F. Mattheiss, *Phys. Rev. B* 13, 2433-2450 (1976).
- [39] J.-W. Rhim, Y.B. Kim, *Phys. Rev. B* 92, 045126 (2015).